# Spin-Transfer-Torque Oscillator with an Antiferromagnetic Exchange-Coupled Composite Free Layer

I. Volvach, A.D. Kent, E.E. Fullerton, and V. Lomakin

Phys. Rev. Applied **18**, 024071 — Published 26 August 2022

DOI: 10.1103/PhysRevApplied.18.024071

# Spin-transfer-torque oscillator with an antiferromagnetic exchange-coupled composite free layer

I. Volvach[1,2], A. D. Kent[3], E. E. Fullerton[1,2], and V. Lomakin[1,2, a)]

[1]Department of Electrical and Computer Engineering, University of California San Diego, La Jolla, CA 92093, USA
[2]Center for Memory and Recording Research, University of California San Diego, La Jolla, CA 92093, USA
[3]Center for Quantum Phenomena, Department of Physics, New York University, NY 10003, USA

We present an antiferromagnetically exchange coupled composite (soft/hard) spin torque oscillator (AF-ECC STO) and demonstrate its operation via both analytical and micromagnetic modeling. The operation exploits the exchange field due to the antiferromagnetic coupling between soft and hard sub-layers of the free layer as well as on the easy-plane anisotropy of the soft sub-layer. Optimized AF-ECC STO structures can generate large amplitude magnetization oscillations, which can be tuned over a broad frequency range with precessions mostly generated by the soft layer. We demonstrate that the AF-ECC STO structure offers flexibility in current control of the oscillation frequency and magnetization angle for realistic material parameters.

## 1. Introduction

Creating broadly tunable microwave and terahertz sources is an ongoing quest for numerous applications, such as high-resolution imaging, nuclear fusion plasma diagnosis, skin cancer screening, large-scale integrated circuit testing, wireless communication among others. Magnetic spin-torque oscillators (STO) are envisioned to offer a number of attractive properties, including high-quality high-frequency microwave generation with broad frequency tunability [1-8] and they can be used for neuromorphic computing and GHz communications [9-11].

STOs typically comprise a reference layer that acts as a spin filter that drives the free layer into a steady-state precession [4-8,12,13]. Additional layers are also introduced for fabrication and measurement, and to optimize material properties. Conventional STOs based on a ferromagnetic free layer have several limitations, such as their highest frequency, which is limited by the saturation magnetization and anisotropy energy density, as well as the general need to have an applied field for a steady precession or to maintain stability and modulate the oscillation frequency range.

There are modified STO configurations that can result in increased precession frequency. In particular, recent reports include theoretical studies based on macrospin models that show that STOs based on an antiferromagnetic free layer (FL) can operate at up to THz frequencies [5-12]. Similar ideas can be extended to using synthetic antiferromagnetic (AF) FLs [5-8]. Reported work [12] using a macrospin approximation showed that synthetic AF free layer can result in high-frequency oscillations due to strong AF exchange. However, such STO configurations have limitations, including a need for an impractically strong AF coupling, lack of a generated microwave field, small precession angle, and narrow frequency/current range of operation.

Here, we present AF exchange-coupled-composite (AF-ECC) STO with perpendicular uniaxial magnetic anisotropy and show its operation via a theoretical model and micromagnetic simulations. The AF-ECC STO is shown in Fig. 1. The FL of the AF-ECC STO is composed of a soft sub-layer (SL) and a hard sub-layer (HL) that are AF coupled through their surfaces with the surface exchange energy density $J_{ex}$. The SL and HL, respectively, have a thickness of $t_s$ and $t_h$, saturation magnetization $M_{s,s}$ and $M_{s,h}$, perpendicular uniaxial anisotropy energy density $K_{u,s}$ and $K_{u,h}$, damping constants $\alpha_s$ and $\alpha_h$, and exchange constants $A_s$ and $A_h$. In addition to the FL with SL and HL, the stack includes a polarizing layer (PL) having $t_{PL}$, $M_{s,PL}$, and $K_{u,PL}$ as well as an AF-coupled read layer (RL) consisting of two sublayers, $RL_1$ and $RL_2$, having $t_{RL1} = t_{RL2}$ and $K_{u,h} = K_{RL1}$, which are AF coupled with $J_{exRL}$. The magnetic layers are separated by spacer layers.

The motivation for the AF-ECC structure is to allow for a tunable precession operation at high frequencies and realistic values of the material and structural parameters, including $J_{ex}$. The operation of the AF-ECC STO is based on the interplay between the effective anisotropy and AF exchange interactions. $K_{u,h}$ is chosen high to maintain a perpendicular effective anisotropy in HL needed for driving SL. On the other hand, $K_{u,s}$ is chosen low such that the FL effectively has an easy-plane anisotropy, which allows driving its large-amplitude precession via the AF exchange.

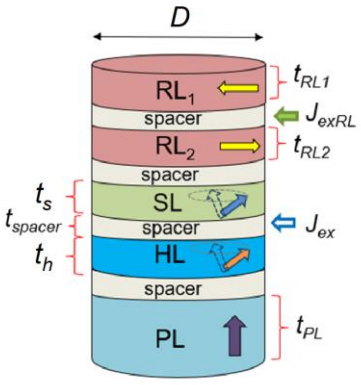


Fig. 1. AF-ECC STO structure.

The PL has a perpendicular anisotropy that is greater than that of the HL to keep it mostly fixed. The magnetostatic fields

a)Electronic mail: vlomakin@eng.ucsd.edu

from the polarizing layer is not compensated, i.e., there is no an AF coupled sublayer to cancel the magnetostatic field from the polarizing layer as often is done for magnetic tunnel junctions (MTJs) used in MRAM [14-16]. The reason for using a single PL is that the effect of the magnetostatic field from PL has an insignificant effect on the STO precession and so there is no need in adding an extra layer. The PL has a perpendicular anisotropy that is greater than that of the HL. The role of the RL is to generate an electric signal by means of tunnel magnetoresistance (TMR). The RL is magnetized in-plane (in the *x*-direction) and the TMR is related to the x-direction of the magnetization in the SL.

All the chosen structure parameters are based on structures and materials used in recent experimental demonstrations of MTJs and spin valve devices [17-21]. The perpendicular anisotropy material of the PL can be composed of a Co/Pt multilayer coupled to a thin CoFeB layer. The HL and SL of the FL can be composed of thinner and thicker CoFeB layers (the perpendicular anisotropy is associated with the CoFeB/MgO interface). The RL can be composed of Co layers. The AF surface exchange coupling can be achieved using Ru or Ir interlayers [17-20]. The dual free layer of the AF-ECC STO structure can be fabricated similar to the recently demonstrated double MTJs [21], showing the feasibility of realizing structures with multiple AF coupled layers.

## 2. Theoretical model

To study the operation of the AF-ECC STO, we first consider a simplified model that includes only the SL and HL of the FL, and the PL is assumed to have a fixed vertical magnetization (see the inset in Fig. 2). We consider a two-spin model, assuming spatially uniform magnetization states in the SL and HL, which are expected to be valid for smaller diameter STOs. We, then, show results of micromagnetic simulations of structures of larger sizes which have the possibility of additional non-uniform dynamics.

In the two-spin approximation, the dynamics can be described by the Landau-Lifshits-Gilbert (LLG) equation [12,22,23] for the two magnetization states

$$\frac{d\mathbf{m}_\xi}{dt} = -\gamma(\mathbf{m}_\xi \times \mathbf{H}_\xi^{eff} + \alpha \mathbf{m}_\xi \times \mathbf{m}_\xi \times \mathbf{H}_\xi^{eff}),$$
$$\mathbf{H}_\xi^{eff} = \beta_\xi \mathbf{m}_\xi \times \mathbf{p} + \frac{J_{ex}}{d_\xi M_{s,\xi}} \mathbf{m}_\varsigma + H_{K,\xi}^{eff} m_{z\xi} \hat{\mathbf{z}}. \quad (1)$$

Here, $\gamma$ is the gyromagnetic ratio, $\mathbf{m}_\xi$ is the normalized magnetization, and $\mathbf{H}_\xi^{eff}$ is the effective field, including the spin-transfer torque (STT), exchange field, and effective anisotropy fields. The subscript $\xi$ is for the HL ($\xi = h$) or SL ($\xi = s$) and the subscript $\varsigma$ is for the other layer, i.e., for $\xi = h$ the value of $\varsigma = s$ and vice versa. The STT component (the first term in the second equation of Eq. (1)) is present only for the HL, i.e., $\beta_s = 0$. For the STT term in the HL, $\mathbf{p}$ is the magnetization of the polarizing layer, which is assumed to be perpendicular, i.e., $\mathbf{p} = \hat{\mathbf{z}}$, and $\beta_h = J\eta\hbar_e/(2eM_{s,h}\delta_h)$ is an STT parameter determining the effective STT field strength, where $J$ is the electric current density, $\eta$ is the spin transfer torque efficiency, $\hbar$ is Planck's constant, $e$ is the electron charge, and $\delta_h$ is the HL thickness. The effective anisotropy field is given by $H_{K,s}^{eff} = K_\xi^{eff} M_{s,\xi}/2$, where $K_\xi^{eff} = K_{u,\xi} - \pi M_{s,\xi}^2 (3N_{z,\xi}/(4\pi) - 1)$ is the effective anisotropy energy density defined in terms of the demagnetization factor $N_{z,\xi}$ [24]. The demagnetization energy and field have an important role in setting the easy axis or easy plane anisotropy. For the chosen material parameters, $H_{K,s}^{eff} < 0$ and $H_{K,h}^{eff} > 0$. On the other hand, the magnetostatic interactions between the layers have only small quantitative effects and, therefore, are excluded from Eq. (1). Additionally, the field-like torque has an insignificant contribution and is also excluded.

The LLG Eq. (1) describes both the initial dynamics and the steady state precession. The steady-state precession can also be characterized by considering the azimuthal ($\varphi$) and elevation ($\theta$) components of the torques. As shown in [25], the dominant torques can be explicitly given by

$$T_{\varphi\xi}^{ex} = -\frac{J_{ex}}{d_\xi M_{s,\xi}} \sin(\theta_h + \theta_s);\ T_{\varphi\xi}^{an} = \frac{H_{K,\xi}^{eff}}{2} \sin(2\theta_\xi),$$
$$T_{\theta\xi}^{ex} = \frac{J_{ex}}{d_\xi M_{s,\xi}} \sin(\phi_\xi - \phi_\varsigma) \sin\theta_\varsigma - \alpha T_{\varphi\xi}^{ex};\ T_{\theta\xi}^{an} = -\alpha T_{\varphi\xi}^{an}, \quad (2)$$
$$T_{\theta h}^{stt} = \beta_h \sin\theta_h$$

in terms of the elevation angles $\theta_s$ and $\theta_h$ as well as azimuthal relative angles $\phi_s$ and $\phi_h$ of the magnetization in the HL and SL, respectively. The rest of the torques can be neglected assuming small $\alpha$. The elevation angles $\theta_s$ and $\theta_h$ have an important role in determining the torques and in determining the magnetization magnitude of the precession in the SL and HL. The relative azimuthal angle $\phi$ has an important role in determining the elevation torque $T_{\theta\xi}^{ex}$ and in the non-uniform magnetization behavior in larger structures, as shown in the micromagnetic analysis.

In order to find the steady-state parameters, we note that the elevation angles $\theta_s$, $\theta_h$, and the relative azimuth angle $\phi = \phi_s - \phi_h - \pi$ are constant as a function of time during the precession; note that the $\pi$ in the definition of $\phi$ is added to characterize the angle shift of $\phi_s$ and $\phi_h$ relative to the mostly $\pi$ angle difference due to the AF coupling. As detailed in [25], the angles $\theta_s$, $\theta_h$, and $\phi$ can be found as solutions to the following system of equations:

$$T_{\theta h}^{ex} + T_{\theta h}^{an} + T_{\theta h}^{stt} = 0,\ \ T_{\theta s}^{ex} + T_{\theta s}^{an} = 0,$$
$$f = \gamma(T_{\varphi h}^{ex} + T_{\varphi h}^{an})/\sin\theta_h = \gamma(T_{\varphi s}^{ex} + T_{\varphi s}^{an})/\sin\theta_s, \quad (3)$$

where the two equations in the first row represent balancing the elevation torques needed for a sustained precessional orbit and the last equation represents the fact that the precessional frequency $f$ in HL and SL is the same.

## 3. Study of the AF-ECC STO operation

In this section, we study the operation of the AF-ECC STO assuming the simplified model, which includes the SL and HL of the FL (as in the inset of Fig. 1). The study incudes the zero-

and room temperature operation. In Sec. 4, we show that the operation of the full stack of Fig. 1 is not altered significantly by the presence of the rest of the stack layers.

### 3.a Operation at zero-temperature

Figure 2 shows $m_z$ in the HL and SL for three values of $J_{ex}$ as a function of $J$. The values $J_{ex}$ are chosen based on using Ru and Ir [17-20]. From Fig. 2(a), for a given $J_{ex}$, $f$ increases with $J$ and reaches the maximal value $f_{\max}$ when $\theta_h$ and $\theta_s$ approach $\pi$. From the analysis of Eqs. (2) and (3), $f_{\max}$ can be approximated by $f_{\max} = -\gamma(2J_{ex}/(d_s M_{s,s}) + H_{K,s}^{eff})$ when assuming that the maximal frequency is obtained for $\theta_h = \theta_s = \pi$. From here, the maximal frequency depends on both $H_{K,s}^{eff}$ and $J_{ex}$, and it can reach values of several hundreds of GHz for large $J_{ex}$ and $H_{K,s}^{eff}$. From Fig. 2(b), for smaller $J_{ex}$, the magnetization of SL has a much greater in-plane component, i.e., it generates a much stronger external magnetic field than that of the HL. With an increase of $J$, $m_z$ of the SL changes its sign from being opposite to the HL direction to the same direction and with a further increase of $J$, the magnetization of SL approaches the perpendicular direction together with that of HL. For greater $J_{ex}$, the magnetization of both the HL and SL are mostly in plane for small $J$ and both approach the perpendicular direction for larger $J$. From Fig. 2(c), the angle $\varphi$ increases with $J$ and decreases with $J_{ex}$.

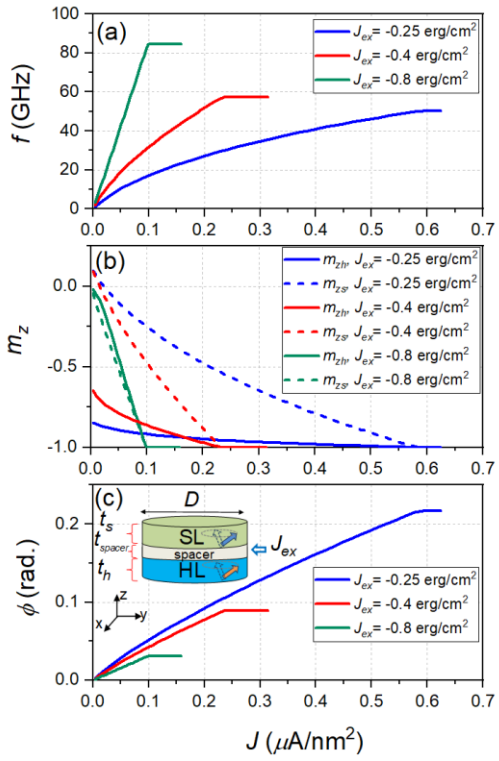


Fig. 2. Inset shows the simplified AF-ECC STO structure. The results obtained via the 2-spin model are shown for (a) $f$, (b) $m_z$, and (c) $\varphi$ as functions of $J$ for different exchange coupling $J_{ex}$ for $D = 20\,\text{nm}$, $t_h = t_s = 0.8\,\text{nm}$, $t_{\text{spacer}} = 0.3\,\text{nm}$, $M_{s,s} = 1350\,\text{emu/cm}^3$, $M_{s,h} = 470\,\text{emu/cm}^3$, $K_{u,h} = 4\,\text{Merg/cm}^3$, $K_{u,s} = 1.11\,\text{Merg/cm}^3$, $\alpha_h = \alpha_s = 0.008$.

To understand the behavior in Fig. 2 and demonstrate the role of different magnetic interactions, Fig. 3 shows the azimuthal and elevation torques for the case of $J_{ex} = -0.4\,\text{erg/cm}^2$. As explained in the model of Eqs. (2) and (3), the elevation torques should balance to zero to maintain a steady-state precession. From Fig. 3(a), the elevation torques in the HL are dominated by the exchange and STT components, which are of an opposite sign maintaining the torque balance. The anisotropy elevation torque component in the HL is relatively insignificant. For the SL (Fig. 3(c)), the elevation torques are dominated by the exchange and effective anisotropy components**,** which are again of an opposite sign maintaining the balance. The exchange elevation torques in the SL and HL have an opposite sign, which explains the same sign of $m_z$ in the HL and SL as shown in Fig. 2(a). The azimuthal torques (Figs. 3(b) and 3(d)) are dominated by exchange and anisotropy components, whereas the STT component is subdominant. The reason for the weak STT contribution is related to the fact that the main role of STT is to overcome the system damping given by $\alpha$, which is small. The azimuthal anisotropy and exchange torques in the HL (Fig. 3(b)) have an opposite sign with the exchange torque dominating. In the SL (Fig. 3(d)), the azimuthal exchange and anisotropy torques are of the same sign and thus they are added to results in the total azimuthal torque. In the steady state, the total azimuthal scaled torques in the HL and SL are the same and they match the precessional frequency in Fig. 2(a), in agreement with the two-spin model of Eqs. (2) and (3).

We also studied the effect of different $\alpha_h$ and $\alpha_s$, and found that an increase of $\alpha_h$ and $\alpha_s$ leads to an increase of the required $J$. The major increase of the required $J$ is due to $\alpha_s$, e.g., to maintain the same $f$ with a double value of $\alpha_s$, $J$ needs to be almost doubled. On the other hand, an increase in $\alpha_h$ has an insignificant effect on the required $J$. This behavior is because $T_{\theta s}^{ex}$ needs to increase to compensate an increase in $T_{\theta s}^{an}$ due to an increased $\alpha_s$, which, in turn, leads to an increase in $T_{\theta h}^{ex}$ and $T_{\theta h}^{stt}$ required for the elevation torque compensation, and hence an increase of $J$. Noting that, typically, soft materials have lower damping constants this behavior constitutes an added benefit [26].

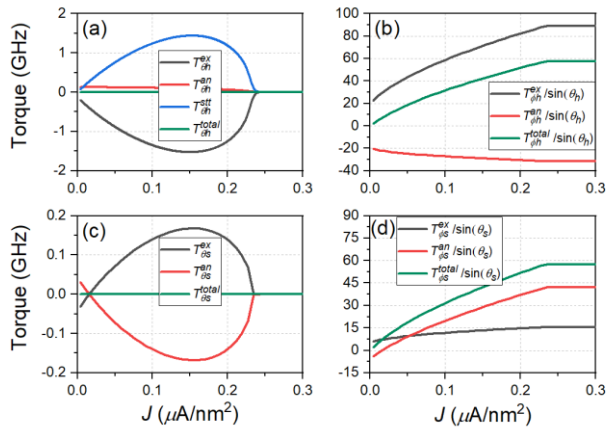


Fig. 3. (a) and (c) elevation torques in the HL and SL; (b) and (d) azimuth torques in the HL and SL. The torques are given for $J_{ex} = -0.4\,\mathrm{erg/cm^2}$ in units of GHz, i.e., they are obtained by multiplying the actual torques by $\gamma$.

We next show results of micromagnetic simulations obtained using the finite element method based micromagnetic simulator FastMag [27]. The maximal edge length of the tetrahedrons in the FEM discretization was chosen to be $<3\,\mathrm{nm}$, which is below the exchange length, to insure spatial convergence. The time stepping is similar to the CVODE package [28] in that it is based on the implicit backward differentiation formulas using adaptive predictor-corrector time stepping, where the time tolerance was chosen as $10^{-5}$ to insure time integration convergence.

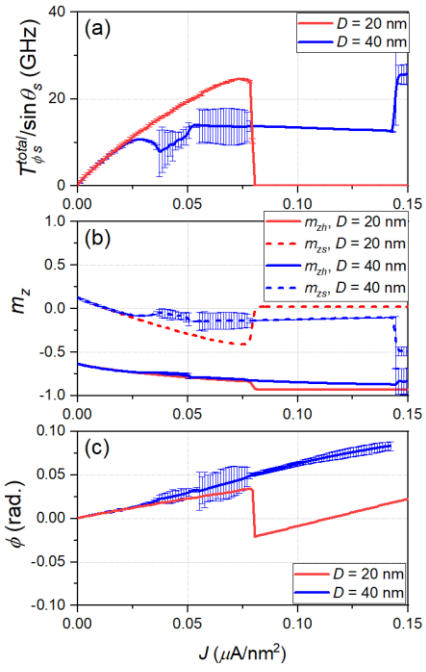


Fig. 4. Micromagnetic results for (a) the average scaled torque $T_{\varphi s}^{total}/\sin\theta_s$, which approximates $f$, (b) averages $m_z$ in the HL and SL, and (c) averaged $\varphi$ as a function of $J$ for $J_{ex} = -0.4\,\mathrm{erg/cm^2}$ for two values of $D = 20\,\mathrm{nm}$ and $40\,\mathrm{nm}$. The remaining parameters are as in Fig. 1 and $A_h = A_s = 1\,\mu\mathrm{erg/cm}$. The bars represent the value spread for a given $J$.

We considered STOs of different sizes and found that the behavior of smaller STOs ($D < 10\,\mathrm{nm}$) is nearly identical to the two-spin model in Figs. 2 and 3, whereas for larger sizes the behavior has more complicated features resulting from magnetization non-uniformities. Figure 4 shows micromagnetic results for the same parameters as in Fig. 2 for $D = 20\,\mathrm{nm}$ and $40\,\mathrm{nm}$ with $J_{ex} = -0.4\,\mathrm{erg/cm^2}$ and Fig. 5 shows the magnetization states corresponding to different responses in Fig. 4. For smaller $J$ the behaviors of all parameters in Fig. 4 are close to those for the two-spin model in Fig. 2 and the precession of the AF-ECC STO is nearly uniform (Fig. 5(a)). For greater $J$ the behavior deviates. For the smaller size of $D = 20\,\mathrm{nm}$, with an increase of $J$, the precession becomes more non-uniform (Fig. 5(b)). At a certain $J$ ($J = 0.15\,\mu\mathrm{A/nm^2}$), the magnetization of the SL goes into a vortex state (Fig. 5(c)), the magnetization of the HL is mostly out of plane, and the precession stops. This behavior can be explained by the azimuthal angle $\phi$ in Fig. 4(c) (and Fig. 2(c)), i.e., for greater $J$, $\phi$ increases and it leads to an increased exchange torques that, in turn, leads to the magnetization twisting resulting in the vortex state. For the greater size, $D = 40\,\mathrm{nm}$, and greater $J$, the precession becomes more non-uniform. The parameters in Fig. 4 have deviations in certain ranges and for larger $J$ (for $J > 0.09\,\mu\mathrm{A/nm^2}$) the precession becomes highly non-uniform and sporadic. As shown in Figs. 5(e and f), the magnetization precessional states change in certain patterns with features of precessing domain walls and vorticies. Figures 4 and 5 are shown for $J_{ex} = -0.4\,\mathrm{erg/cm^2}$, which is a practical value for Ru [17]. For a greater $J_{ex} = -0.8\,\mathrm{erg/cm^2}$, which can be achieved with, e.g., Ir [19], the behavior is qualitatively similar but the range of $J$ with uniform precession is broader and the precessional frequency is greater.

To further demonstrate the achievable frequency range, Fig. 6 shows the micromagnetic results of the precession frequency for the same parameters as in Fig. 4 for $D = 20\,\mathrm{nm}$ and $40\,\mathrm{nm}$ for different values of $J_{ex}$. It is found that the maximal achievable frequency increases with an increase of $J_{ex}$. In particular, for $J_{ex} = -1.5\,\mathrm{erg/cm^2}$, which can be obtained, e.g., with Ir [19], the precessional frequency can be above 100 GHz. For even greater $J_{ex} = -3\,\mathrm{erg/cm^2}$, the frequency can be above 200 GHz; such large values of $J_{ex}$ can be obtained using, for instance, Fe1-xSix spacers [29] or direct coupling of rare-earth-transition-metal alloy layers to transition metal layers [30].

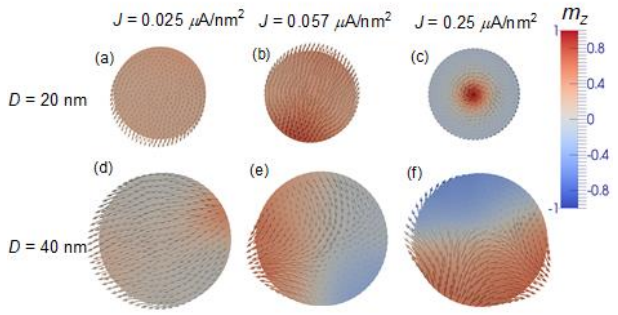


Fig. 5. Snapshots of $m_z$ of the SL for $J_{ex} = -0.4\,\mathrm{erg/cm^2}$ for $D = 20\,\mathrm{nm}$ and $40\,\mathrm{nm}$ for different $J$. The rest of the parameters are as in Figs. 1 and 3. Videos showing the magnetization dynamics are provided for a linearly increasing $J$ in a range of 0 to $0.12\,\mu\mathrm{A/nm^2}$ over the time frame of $2\,\mu\mathrm{s}$ [31].

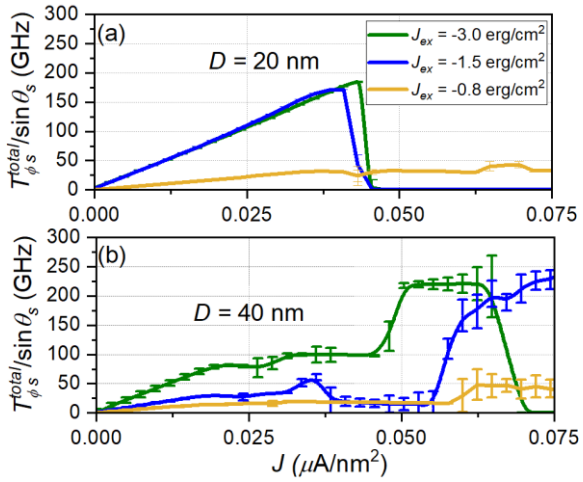


Fig. 6. Micromagnetic results for (a) the average scaled torque $T_{\varphi s}^{total}/\sin\theta_s$, which approximates $f$ for different $J_{ex}$ for (a) $D = 20\,\mathrm{nm}$ and (b) $40\,\mathrm{nm}$. The remaining parameters are as in Fig. 1 and $A_h = A_s = 1\,\mu\mathrm{erg/cm}$. The bars represent the value spread for a given $J$.

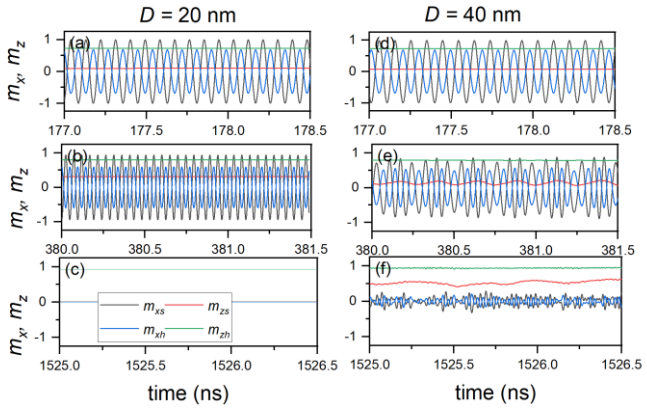


Fig. 7. Time dependence of the normalized magnetization components $m_x$ and $m_z$ for different $J$ in the SL and HL for $J_{ex} = -0.4\,\mathrm{erg/cm^2}$ for $D = 20\,\mathrm{nm}$ and $40\,\mathrm{nm}$. For (a) and (d) $J = 0.025\,\mu\mathrm{A/nm^2}$, for (b) and (e) $J = 0.057\,\mu\mathrm{A/nm^2}$, and for (c), (f) $J = 0.25\,\mu\mathrm{A/nm^2}$. The remaining parameters are as in Figs. 2 and 4.

Figure 7 shows the averaged $m_x$ and $m_z$ in the SL and HL for $D = 20\,\mathrm{nm}$ and $40\,\mathrm{nm}$ for different values of $J$. At the smallest shown $J$ (Figs. 7(a) and (d)), the behavior of $m_x$ and $m_z$ for $D = 20\,\mathrm{nm}$ and $40\,\mathrm{nm}$ is nearly the same: the precession is uniform with mostly in-plane precession in the SL and smaller amplitude precession in the HL, which corresponds to mostly uniform profiles in Figs. 5(a) and (d). At a greater $J$ and $D = 20\,\mathrm{nm}$, the SL still has a uniform precession with a higher frequency (Fig. 7(b)), whereas for $D = 40\,\mathrm{nm}$ the precession becomes partially non-uniform with a lower frequency (Fig. 7(e)). At the highest $J$, for $D = 20\,\mathrm{nm}$ the SL does not precess (Fig. 7(c)), which corresponds to the vortex state as shown in Fig. 5(c). At the same highest $J$, for $D = 40\,\mathrm{nm}$ the HL has a highly non-uniform precession (Fig. 7(f)), which corresponds to the spatial magnetization profile of Fig. 7(f).

### 3.b Operation at room temperature

Characterizing thermal noise is important for understanding the operation of STOs finite temperatures. Here, we show results of the micromagnetic analysis of the AF-ECC STO at room temperature $T = 300\,K$. The micromagnetic simulation were performed with the FastMag simulator that included stochastic effects [32,33]. The remaining simulation parameters were as in Sec. 3.a.

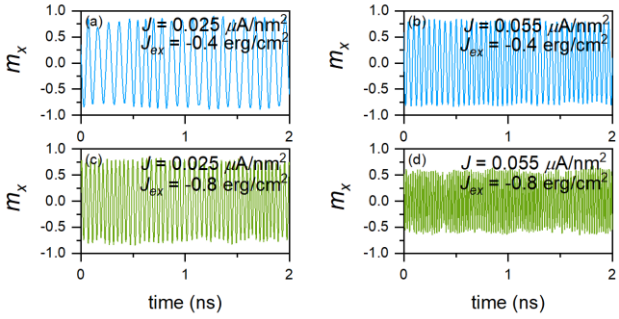


Fig. 8. Magnetization component $m_x$ vs time at room temperature for different $J$ and $J_{ex}$.

Figure 8 shows the magnetization dynamics in the FL for different $J$ and $J_{ex}$. The time dependence shows precession as at zero temperature but the precessional amplitude and frequency have some random variations. Figure 9 shows the Fourier spectrum corresponding to the time dynamics results in Fig. 8. The spectrum has a maximum at the frequency corresponding to the zero-temperature frequency. The linewidth depends on the choice of the structure parameters. Generally, we find that higher $J$ and $J_{ex}$, which correspond to higher precessional frequencies, lead to a narrower linewidth. This behavior is important as one of the benefits of the AF-ECC STO is its high-frequency operation.

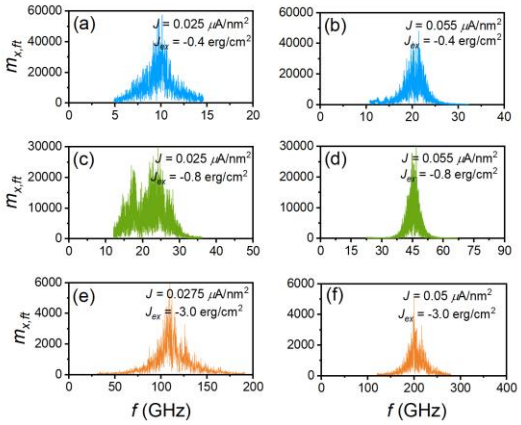


Fig. 9. Fourier spectrum of $m_x$ for the operation at room temperature for different $J$ and $J_{ex}$ for the AF-ECC STO for $D = 40\,\text{nm}$.

We then compare the room temperature operation of the AF-ECC STO with the operation of other STO types, including an easy-plane single-FL STO, which is chosen as it can operate without an applied field [34], and an easy-axis STO with an applied field, which is chosen as it was the original concept for an STO [35-38]. Both STOs chosen for comparison operate only at lower frequency ranges that those typical of the AF-ECC STO and, therefore, the comparisons are done at the lower frequency range.

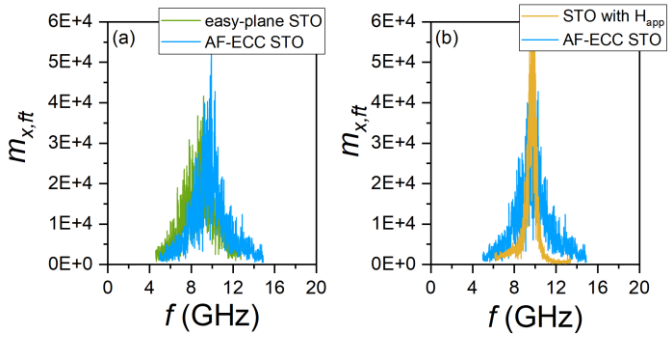


Fig. 10. Fourier spectrum of $m_x$ for the operation at room temperature of an AF-ECC STO with $J_{ex} = -0.4\,\text{erg/cm}^2$ and $J = 0.04\,\mu\text{A/nm}^2$ icompared to (a) easy-plane single-FL STO with the following parameters: thickness $t = 0.8\,\text{nm}$, $M_s = 1350\,\text{emu/cm}^3$, $K_u = 1.11\,\text{Merg/cm}^3$, $J = 0.04\,\mu\text{A/nm}^2$, $\alpha = 0.008$; (b) easy-axis STO with an applied field with the following parameters: $t = 3.0\,\text{nm}$, $M_s = 1350\,\text{emu/cm}^3$, $K_u = 1.11\,\text{Merg/cm}^3$, $\alpha = 0.008$, $J = 0.01\,\mu\text{A/nm}^2$ and $H_{app} = 0.4\,\text{T}$. For all cases $D = 40\,\text{nm}$.

Figures 10 (a) and (b) compare the frequency spectrum of AF-ECC STO with those of the easy-plane single-FL STO and easy-axis STO with an applied field, respectively. The structure parameters of the STOs are chosen such that they operate at the same frequency at zero-temperature. We find that the linewidth of the easy-plane single-FL STO is about the same as that of the AF-ECC STO (Fig. 10(a)). On the other hand, the linewidth of the easy-axis STO with an applied field is narrower (Fig. 10(b)). We attribute the reduced linewidth in the latter case to the fact that the precessional frequency is largely given by the applied field that is temperature and thermal noise independent. On the other hand, for the AF-ECC STO and easy-plane single-FL STO, the precessional frequency is determined by the anisotropy and exchange interactions. These interactions are affected by the thermal noise because they are related to the instantaneous magnetization states, which are a part of the stochastic magnetization dynamics. We note that the linewidth can be reduced by synchronizing multiple STOs or synchronizing the STOs to an AC current or external field [39-41].

## 4. Effect of the full AF-ECC STO stack

In this section, we demonstrate the effects of the full stack on the operation of the AF-ECC STO as it would be fabricated for using the AF-ECC STO to generate an electric signal (Fig. 1).

The PL experiences an STT from the HL, which is given by the expression as in the STT component of Eq. (1), where $\mathbf{p}$ is replaced with the magnetization HL and $\mathbf{m}_\xi$ is replaced with the magnetization of the PL. Because of this torque, magnetostatic interactions, and the finite PL anisotropy the magnetization of the PL can move, but, as we show next, this motion is insignificant. There is also STT acting on the SL due to $RL_2$. The STT efficiencies are the same for all STT components. The spacer layer is assumed to have the same thickness of $t_{\text{spacer}}$.

Table 1. Precessional frequency of the 2-layer stack and full stack for $J = 0.025\,\mu\text{A/nm}^2$ for different $D$ and $J_{ex}$. The material parameters are chosen as $t_h = t_s = 0.8\,\text{nm}$, $t_{RL1} = t_{RL2} = 2.4\,\text{nm}$, $t_{PL} = 4.0\,\text{nm}$, $t_{\text{spacer}} = 0.3\,\text{nm}$, $M_{s,s} = 1350\,\text{emu/cm}^3$, $M_{s,PL} = 900\,\text{emu/cm}^3$, $M_{s,h} = M_{s,RL1} = M_{s,RL2} = 470\,\text{emu/cm}^3$, $K_{u,h} = K_{RL1} = K_{RL2} = 4\,\text{Merg/cm}^3$, $K_{u,s} = 1.11\,\text{Merg/cm}^3$, $K_{u,PL} = 6.11\,\text{Merg/cm}^3$, $\alpha_h = \alpha_s = \alpha_{RL1} = \alpha_{RL2} = \alpha_{PL} = 0.008$, $J_{exRL} = -0.12\,\text{erg/cm}^2$, $\beta_f = 0.3$.

| $J_{ex}$, erg/cm² | $f$, GHz | | | |
|---|---|---|---|---|
| | 2-layer, $D = 20\,\text{nm}$ | Full stack, $D = 20\,\text{nm}$ | 2-layer, $D = 40\,\text{nm}$ | Full stack, $D = 40\,\text{nm}$ |
| -0.25 | 6.0 | 5.4 | 5.9 | 5.7 |
| -0.4 | 11.0 | 10.0 | 10.5 | 9.9 |
| -0.8 | 22.7 | 20.4 | 15.0 | 13.7 |

Table 1 compares the precessional frequency of the simplified 2-layer stack and full stack of Fig. 1 for different $D$ and $J_{ex}$. The results show around 10% difference in the precessional frequency. Otherwise, the behavior of all the parameters for the 2-layer and full stack is the same. The difference is related to the magnetostatic and field-like torques, which are relatively weak. Additional details on the relative strengths of the magnetostatic and field-like torques are given in [25].

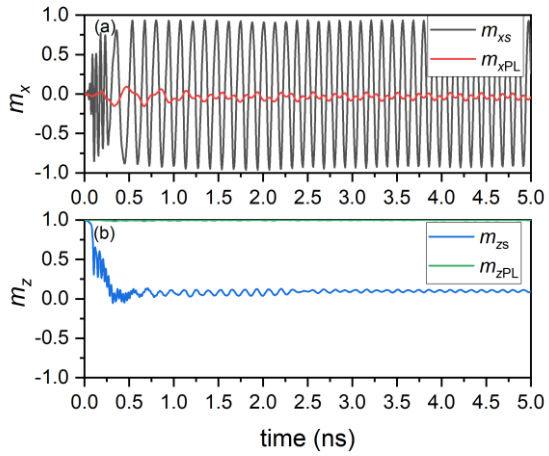


Fig. 11. Time dependence of the normalized magnetization components $m_x$ and $m_z$ in SL and PL for $J_{ex} = -0.4\,\mathrm{erg/cm^2}$ and $J = 0.035\,\mu\mathrm{A/nm^2}$. The dynamics in PL occurs due to its finite anisotropy combined with the STT and magnetostatic interactions. The material parameters are as in Table 1.

The results in Table 1 include effects of the STT at PL due to the HL and at the SL due to the $RL_2$ but their influence on the frequency is insignificant. Figure 11 further demonstrates the effects of the mutual torque and magnetostatic interactions in PL and HL. These interactions make the PL move, which also affects the oscillations in the HL and SL. However, these effects are weak, and they do not change any conclusions about the feasibility of practical use of the AF-ECC STO.

We further note that the effects of STTs at the SL due to the RL are diminishing, which can be explained by the fact that the precession of the SL is in-plane, and it has a high frequency. The main STT effect is in the damping component, which is averaged and cancelled out while the high-frequency SL precession to result in no influence on the operation of the STO.

We note that the effects of the magnetostatic and field-like torques can be further reduced by adding an AF-coupled sublayer to the PL, which can be tuned to cancel the effects of both the PL and field-like torques. However, since the obtained effects are already weak, we do not introduce additional complications in the stack design.

Finally, we note that the current density levels required for the operation of the presented AF-ECC STO are below $0.1\,\mu\mathrm{A/nm^2}$. These current density levels are consistent with what was demonstrated in recent experimental works using similar MTJ structures and materials [42]. The expected generated power can be estimated based on the parallel and antiparallel FL-RL magnetoresistance values. For instance, assuming a magnetoresistance of 400 Ohms and 1400 Ohms for the parallel and anti-parallel FL – RL states, respectively, [43], assuming a large-angle precession for the current of 0.1 mA, which is obtained for $D = 40\,\mathrm{nm}$ with $J = 0.08\,\mu\mathrm{A/nm^2}$, the generated power is estimated as $2.5\,\mu\mathrm{W}$. This power level is consistent with recent experimental works demonstrating STOs with MTJs, and it can be increased when the STOs are synchronized in an array [42].

## 5. Summary

We presented an AF-ECC STO, which has its FL composed of AF coupled SL and HL. The easy-plane anisotropy of the SL allows the operation at realistic AF coupling strengths producing large precession angles, which is important for generating a large signal. We developed an analytical model based on a two-spin approximation and further used micromagnetics to study size effects.

The precessional frequency can be tuned in a broad frequency range. The operation of the STO can be understood from an interplay between the exchange and anisotropy interactions. The magnetizations in the SL and HL have an azimuthal angular shift, which plays an important role in setting the precessional angle and frequency. The micromagnetic study shows that for smaller currents the operation is close to that predicted by the two-spin model, whereas for greater currents the precessional motion becomes non-uniform.

We studied the operation of the AF-ECC STO at zero-temperature as well as at room temperature, which includes stochastic thermal noise effects. The linewidth of the Fourier spectrum of the magnetization is higher for greater current densities and AF exchange energy densities, which correspond to higher operational frequencies. The linewidth of the AF-ECC STO is greater than that of an easy-axis STO with an applied field and similar to an easy-plane single-FL STO.

AF-ECC STO can be used to generate tunable high-frequency electric signals or to generate an oscillating magnetic field for applications such as microwave assisted magnetic recording. In the latter case, there is no need in the RL layers. A microwave field can be generated because the precession magnetization magnitude in the SL can be greater than that in the HL.

*Acknowledgments.* This work was supported as part of the Quantum-Materials for Energy Efficient Neuromorphic-Computing (Q-MEEN-C), an Energy Frontier Research Center funded by the U.S. Department of Energy, Office of Science, Basic Energy Sciences under Award No. DE-SC0019273. This work used the XSEDE [44], which is supported by NSF grant number ACI-1548562, specifically, it used the Bridges and Comet systems supported by NSF Grant # ACI-1445506.

The data that support the findings of this study are available from the corresponding author upon reasonable request.

## References

[1] A. Slavin and V. Tiberkevich, Nonlinear Auto-Oscillator Theory of Microwave Generation by Spin-Polarized Current, IEEE Trans. Magn. **45** (4), 1875 (2009).

[2] S. I. Kiselev, J. C. Sankey, I. N. Krivorotov, N. C. Emley, R. J. Schoelkopf, R. A. Buhrman, and D. C. Ralph, Microwave oscillations of a nanomagnet driven by a spin-polarized current, Nature **425** (6956), 380 (2003).

[3] S. I. Kiselev, J. C. Sankey, I. N. Krivorotov, N. C. Emley, M. Rinkoski, C. Perez, R. A. Buhrman, and D. C. Ralph, Current-induced nanomagnet dynamics for

magnetic fields perpendicular to the sample plane, Physical Review Letters **93** (3) (2004).

[4] S. I. Kiselev, J. C. Sankey, I. N. Krivorotov, N. C. Emley, A. G. F. Garcia, R. A. Buhrman, and D. C. Ralph, Spin-transfer excitations of permalloy nanopillars for large applied currents, Phys. Rev. B **72** (6) (2005).

[5] V. Puliafito, R. Khymyn, M. Carpentieri, B. Azzerboni, V. Tiberkevich, A. Slavin, and G. Finocchio, Micromagnetic modeling of terahertz oscillations in an antiferromagnetic material driven by the spin Hall effect, Phys. Rev. B **99** (2) (2019).

[6] R. Khymyn, I. Lisenkov, V. Tiberkevich, B. A. Ivanov, and A. Slavin, Antiferromagnetic THz-frequency Josephson-like Oscillator Driven by Spin Current, Scientific Reports **7** (2017).

[7] R. Khymyn, I. Lisenkov, V. S. Tiberkevich, A. N. Slavin, and B. A. Ivanov, Transformation of spin current by antiferromagnetic insulators, Phys. Rev. B **93** (22) (2016).

[8] C. Safranski and J. Z. Sun, Interface moment dynamics and its contribution to spin-transfer torque switching process in magnetic tunnel junctions, Phys. Rev. B **100** (1) (2019).

[9] J. Torrejon, M. Riou, F. A. Araujo, S. Tsunegi, G. Khalsa, D. Querlioz, P. Bortolotti, V. Cros, K. Yakushiji, A. Fukushima, H. Kubota, S. Y. Uasa, M. D. Stiles, and J. Grollier, Neuromorphic computing with nanoscale spintronic oscillators, Nature **547** (7664), 428 (2017).

[10] J. Grollier, D. Querlioz, and M. D. Stiles, Spintronic Nanodevices for Bioinspired Computing, Proceedings of the Ieee **104** (10), 2024 (2016).

[11] J. A. Katine and E. E. Fullerton, Device implications of spin-transfer torques, J. Magn. Magn. Mater. **320** (7), 1217 (2008).

[12] H. Zhong, S. Z. Qiao, S. S. Yan, L. J. Liang, Y. R. Zhao, and S. S. Kang, Terahertz spin-transfer torque oscillator based on a synthetic antiferromagnet, J. Magn. Magn. Mater. **497** (2020).

[13] D. Houssameddine, J. F. Sierra, D. Gusakova, B. Delaet, U. Ebels, L. D. Buda-Prejbeanu, M. C. Cyrille, B. Dieny, B. Ocker, J. Langer, and W. Maas, Spin torque driven excitations in a synthetic antiferromagnet, Appl. Phys. Lett. **96** (7) (2010).

[14] Y. Tomczak, T. Lin, J. Swerts, S. Couet, S. Mertens, E. L. Liu, W. Kim, K. Sankaran, G. Pourtois, D. Tsvetanova, L. Souriau, S. Van Elshocht, G. S. Kar, and A. Furnemont, Influence of the Reference Layer Composition on the Back-End-of-Line Compatibility of Co/Ni-Based Perpendicular Magnetic Tunnel Junction Stacks, IEEE Trans. Magn. **52** (7) (2016).

[15] A. V. Khvalkovskiy, D. Apalkov, S. Watts, R. Chepulskii, R. S. Beach, A. Ong, X. Tang, A. Driskill-Smith, W. H. Butler, P. B. Visscher, D. Lottis, E. Chen, V. Nikitin, and M. Krounbi, Basic principles of STT-MRAM cell operation in memory arrays (vol 46, 074001, 2013), J. Phys. D Appl. Phys. **46** (13) (2013).

[16] D. Apalkov, B. Dieny, and J. M. Slaughter, Magnetoresistive Random Access Memory, Proceedings of the Ieee **104** (10), 1796 (2016).

[17] L. Fallarino, V. Sluka, B. Kardasz, M. Pinarbasi, A. Berger, and A. D. Kent, Interlayer exchange coupling between layers with perpendicular and easy-plane magnetic anisotropies, Appl. Phys. Lett. **109** (8) (2016).

[18] O. Hellwig, A. Berger, and E. E. Fullerton, Magnetic phase separation in artificial A-type antiferromagnetic films, Phys. Rev. B **75** (13) (2007).

[19] O. Hellwig, A. Berger, J. B. Kortright, and E. E. Fullerton, Domain structure and magnetization reversal of antiferromagnetically coupled perpendicular anisotropy films, J. Magn. Magn. Mater. **319** (1-2), 13 (2007).

[20] S. S. P. Parkin, N. More, and K. P. Roche, Oscillations in Exchange Coupling and Magnetoresistance in Metallic Superlattice Structures - Co/Ru, Co/Cr, and Fe/Cr, Physical Review Letters **64** (19), 2304 (1990).

[21] G. Hu, G. Lauer, J. Z. Sun, P. Hashemi, C. Safranski, S. L. Brown, L. Buzi, E. R. J. Edwards, C. P. D'Emic, E. Galligan, M. G. Gottwald, O. Gunawan, H. Jung, J. Kim, K. Latzko, J. J. Nowak, P. L. Trouilloud, S. Zare, and D. C. Worledge, 2X reduction of STT-MRAM switching current using double spin-torque magnetic tunnel junction, 2021 Ieee International Electron Devices Meeting (Iedm) (2021).

[22] J. C. Slonczewski, Current-driven excitation of magnetic multilayers, J. Magn. Magn. Mater. **159** (1-2), L1 (1996).

[23] L. Berger, Emission of spin waves by a magnetic multilayer traversed by a current, Phys. Rev. B **54** (13), 9353 (1996).

[24] G. M. Wysin, Magnetic Excitations and Geometric Confinement: Theory and Simulations, Magnetic Excitations and Geometric Confinement: Theory and Simulations, 1 (2015).

[25] See Supplemental Material at [URL will be inserted by publisher] for derivation of Eqs. (2)-(3) and torque strengths.

[26] I. Yulaev, M. V. Lubarda, S. Mangin, V. Lomakin, and E. E. Fullerton, Spin-transfer-torque reversal in perpendicular anisotropy spin valves with composite free layers, Appl. Phys. Lett. **99** (13) (2011).

[27] R. Chang, S. Li, M. V. Lubarda, B. Livshitz, and V. Lomakin, FastMag: Fast micromagnetic simulator for complex magnetic structures (invited) (vol 109, 07D358, 2011), J. Appl. Phys. **110** (3) (2011).

[28] R. Serban and A. C. Hindmash, CVODES, the sensitivity-enabled ODE solver in SUNDIALS, Proceedings of the Asme International Design Engineering Technical Conferences and Computers and Information in Engineering Conference, Vol 6, Pts a-C, 257 (2005).

[29] R. R. Gareev, D. E. Burgler, M. Buchmeier, R. Schreiber, and P. Grunberg, Very strong interlayer exchange coupling in epitaxial Fe/Fe1-xSix/Fe trilayers (x=0.4-1.0), J. Magn. Magn. Mater. **240** (1-3), 235 (2002).

[30] S. M. Watson, T. Hauet, J. A. Borchers, S. Mangin, and E. E. Fullerton, Interfacial magnetic domain wall formation in perpendicular-anisotropy, exchange-spring films, Appl. Phys. Lett. **92** (20) (2008).

[31] Videos of the magnetization dynamics for D = 20 nm (hyperlink to video 1) and D = 40 nm (hyperlink to video 2) in Fig. 5.

[32] D. J. Dunlop, Magnetism in Rocks, Journal of Geophysical Research-Solid Earth **100** (B2), 2161 (1995).

[33] D. V. Berkov and N. L. Gorn, Stochastic dynamic simulations of fast remagnetization processes: recent advances and applications, J. Magn. Magn. Mater. **290**, 442 (2005).

[34] D. Houssameddine, U. Ebels, B. Delaet, B. Rodmacq, I. Firastrau, F. Ponthenier, M. Brunet, C. Thirion, J. P. Michel, L. Prejbeanu-Buda, M. C. Cyrille, O. Redon, and B. Dieny, Spin-torque oscillator using a perpendicular polarizer and a planar free layer, Nature Materials **6** (6), 447 (2007).

[35] I. Firastrau, L. D. Buda-Prejbeanu, B. Dieny, and U. Ebels, Spin-torque nano-oscillator based on a synthetic antiferromagnet free layer and perpendicular to plane polarizer, J. Appl. Phys. **113** (11) (2013).

[36] Z. M. Zeng, G. Finocchio, and H. W. Jiang, Spin transfer nano-oscillators, Nanoscale **5** (6), 2219 (2013).

[37] M. d'Aquino, C. Serpico, G. Bertotti, R. Bonin, and I. D. Mayergoyz, Analysis of thermally induced magnetization dynamics in spin-transfer nano-oscillators, Physica B-Condensed Matter **407** (9), 1389 (2012).

[38] R. Sato, Y. Saito, and K. Mizushima, Current-dependent linewidth of a spin-transfer nano-oscillator, J. Magn. Magn. Mater. **321** (8), 990 (2009).

[39] M. d'Aquino, C. Serpico, R. Bonin, G. Bertotti, and I. D. Mayergoyz, Analysis of synchronized regimes for injection-locked spin-transfer nano-oscillators, Physica B-Condensed Matter **407** (9), 1357 (2012).

[40] M. d'Aquino, C. Serpico, R. Bonin, G. Bertotti, and I. D. Mayergoyz, Micromagnetic study of phase-locking in spin-transfer nano-oscillators driven by currents and ac fields, J. Appl. Phys. **109** (7) (2011).

[41] K. N. Aleshin, V. V. Matrosov, and K. G. Mishagin, Synchronization of Spin-Transfer Nano-Oscillator by an External Source, Technical Physics Letters **43** (3), 281 (2017).

[42] R. Sharma, R. Mishra, T. Ngo, Y. X. Guo, S. Fukami, H. Sato, H. Ohno, and H. Yang, Electrically connected spin-torque oscillators array for 2.4GHz WiFi band transmission and energy harvesting, Nature Communications **12** (1) (2021).

[43] M. X. Wang, W. L. Cai, K. H. Cao, J. Q. Zhou, J. Wrona, S. Z. Peng, H. W. Yang, J. Q. Wei, W. Kang, Y. G. Zhang, J. Langer, B. Ocker, A. Fert, and W. S. Zhao, Current-induced magnetization switching in atom-thick tungsten engineered perpendicular magnetic tunnel junctions with large tunnel magnetoresistance, Nature Communications **9** (2018).

[44] J. Towns, T. Cockerill, M. Dahan, I. Foster, K. Gaither, A. Grimshaw, V. Hazlewood, S. Lathrop, D. Lifka, G. D. Peterson, R. Roskies, J. R. Scott, and N. Wilkins-Diehr, XSEDE: Accelerating Scientific Discovery, Comput. Sci. Eng. **16** (5), 62 (2014).